

To appear in *Astrophysical Journal*

The sources of HCN and CH₃OH and the Rotational Temperature in Comet 103P/Hartley 2 from Time-Resolved Millimeter Spectroscopy*

Michał Drahus, David Jewitt, and Aurélie Guilbert-Lepoutre

*Department of Earth and Space Sciences, University of California at Los Angeles,
Los Angeles, CA 90095*

mdrahus@ucla.edu

Wacław Waniak

Astronomical Observatory, Jagiellonian University, Kraków, Poland

and

Albrecht Sievers

Instituto de Radio Astronomía Milimétrica, Granada, Spain

ABSTRACT

One of the least understood properties of comets is the compositional structure of their nuclei, which can either be homogeneous or heterogeneous. The nucleus structure can be conveniently studied at millimeter wavelengths, using velocity-resolved spectral time series of the emission lines, obtained simultaneously for multiple molecules as the body rotates. Using this technique, we investigated the sources of CH₃OH and HCN in comet 103P/Hartley 2, the target of NASA's *EPOXI* mission, which had an exceptionally favorable apparition in late 2010. Our monitoring at IRAM 30-m shows short-term variability of the spectral lines caused by nucleus rotation. The varying production rates generate changes in brightness by a factor of 5 for HCN and by a factor of 2 for CH₃OH, and they are remarkably well correlated in time. With the addition of the velocity information from the line profiles, we identify the main sources of outgassing: two jets, oppositely directed in a radial sense, and icy grains, injected into the coma primarily through one of the jets. The mixing ratio of CH₃OH and HCN is dramatically different in the two jets, which evidently shows large-scale chemical heterogeneity of the nucleus. We propose a network of identities linking the two jets with morphological

*Based on observations carried out with the IRAM 30 m telescope. IRAM is supported by INSU/CNRS (France), MPG (Germany), and IGN (Spain).

features reported elsewhere, and postulate that the chemical heterogeneity may result from thermal evolution. The model-dependent average production rates are 2.10×10^{26} molec s⁻¹ for CH₃OH and 1.25×10^{25} molec s⁻¹ for HCN and their ratio is typical of comets. The rotational temperature from CH₃OH varied strongly, presumably due to nucleus rotation, with the average value 47 K.

Subject headings: comets: general — comets: individual (103P) — radio lines: general

1. Introduction

Comets are icy remnants holding clues about the formation and evolution of the Solar system. Depending on the region of formation in the protosolar nebula, they are currently stored in two main reservoirs: the Oort cloud and the Kuiper belt. The Oort cloud is a source of long-period comets and (probably) Halley-type comets (Levison 1996). It has been suggested that Oort cloud comets formed in the giant planet region and were subsequently ejected to the periphery of the Solar system (e.g. Dones et al. 2004), but also that some may have been captured from other stellar systems while the Sun was in its birth cluster (Levison et al. 2010). The Kuiper belt is a source of Jupiter-family comets (e.g. Duncan et al. 2004). Kuiper belt comets presumably formed just beyond the orbit of Neptune where they continue to orbit. By studying comets from different reservoirs we can probe the different environments in which they formed, and also better understand their role in the Solar system as the suppliers of water and organics.

103P/Hartley 2 (hereafter 103P) is a Jupiter-family comet which currently has a 6.47-year orbital period and perihelion at 1.06 AU. On UT 2010 Oct. 20.7 it reached the minimum geocentric distance of only 0.12 AU, making by far the closest approach to the Earth since its discovery (Hartley 1986), and becoming visible to the naked eye. Shortly after, on UT 2010 Nov. 4.5832, the comet was visited by NASA’s *EPOXI* spacecraft, which provided detailed images and spectra of the nucleus and its closest surroundings (A’Hearn et al. 2011). Both the Earth-based data, taken at an unusually favorable geometry, and the unique observations carried out by the spacecraft, create an exceptional platform for new groundbreaking investigations.

One of the most fundamental problems of cometary science is the compositional structure of the nucleus, which holds unique information about the formation and evolution of comets. A nucleus which condensed in one place would be, at least initially, homogeneous and compositionally similar to that region of the protosolar nebula. In contrast, a heterogeneous composition would suggest formation from smaller “cometesimals” which accumulated into comets in the early Solar system. Because of the expected radial migration of cometesimals (Weidenschilling 1977), they could originate at different heliocentric distances in the protosolar disk and hence have different chemical compositions. The above interpretation can be biased, to some extent, for thermally-evolved comets, in which depletion in the most volatile ices may occur non-uniformly (Guilbert-Lepoutre & Jewitt 2011).

Both homogeneous (e.g. Dello Russo et al. 2007) and heterogeneous (e.g. Gibb et al. 2007) compositions have been suggested for different comets based on ground-based IR spectroscopy of the emission lines. The best information, however, came from the spatially-resolved molecular images of water (H_2O) and carbon dioxide (CO_2), obtained for comets 9P/Tempel 1 and 103P within the *Deep Impact* and *EPOXI* missions, respectively (Feaga et al. 2007; A’Hearn et al. 2011). These observations showed that each comet emit the two molecules from distinct sources at different locations on their nuclei. But ground-based IR spectroscopy of 103P (Mumma et al. 2011; Dello Russo et al. 2011) did not provide any compelling evidence for similar differences among other molecules, including methanol (CH_3OH) and hydrogen cyanide (HCN). We address this issue in detail in this work, using our own millimeter-wavelength observations of CH_3OH and HCN in this comet.

Millimeter-wavelength spectroscopy is a powerful tool with which to investigate comets, because it is sensitive to parent molecules through their rotational transitions and because the spectra are velocity-resolved. A time series of velocity-resolved spectra, obtained simultaneously for multiple molecules, reveal their production rates and line-of-sight kinematics over the course of the nucleus rotation. We can thereby identify if these molecules originate from the same source(s) or from different sources (compositional homogeneity vs. heterogeneity), and in this way gain rare and valuable insights into the compositional structure of the nucleus. Moreover, millimeter spectroscopy provides excellent diagnostics of the rotational temperature in the coma, which can be derived from simultaneous observations of different transitions from the same molecule.

In the present paper we continue the exploration of our mm/submm spectroscopic observations of 103P obtained in late 2010. Earlier we quantified the rotation state of the nucleus based on an extensive monitoring of the HCN line variability observed at multiple telescopes (Drahus et al. 2011, hereafter Paper I). This time we focus on a small but unique subset of data from a single instrument to investigate the sources of CH_3OH and HCN . Using the former molecule, we also constrain time-resolved rotational temperature. Our findings presented in Paper I have been accounted for in the present work, in particular, we now average the spectra in longer, 1-hr blocks (vs. 15 min in Paper I), to increase the signal-to-noise ratio. This change is motivated by the fact that the nucleus rotation period, equal to 18.33-hr at the epoch of observations (cf. Paper I; also e.g. A’Hearn et al. 2011), is long-enough to prevent any significant variability on timescales shorter than an hour. Moreover, we analyze the spectra in 0.15 km s^{-1} bins (vs. 0.10 and 0.25 km s^{-1} in Paper I), which is limited by the native resolution available for CH_3OH . While we are generally consistent with the methodology used in Paper I, in the current work we calculate the line parameters from a narrower window (from -1.75 to $+1.75 \text{ km s}^{-1}$ instead of from -2 to $+2 \text{ km s}^{-1}$) to further improve the signal-to-noise ratio, and derive the molecular production rates using a revised rotational temperature (47 K from CH_3OH at the epoch of observations, instead of 30 K obtained previously from long-term monitoring of HCN at various telescopes).

2. Observations and Data Reduction

We took observations at the 30-m millimeter telescope on Pico Veleta (Spain), operated by the Institut de Radioastronomie Millimétrique (IRAM). On three consecutive nights: UT 2010 Nov. 3.03–3.35, Nov. 4.03–4.34, and Nov. 5.02–5.35, we obtained time series of velocity-resolved spectra of CH₃OH and HCN. The middle moment of these time series (hereafter the epoch of observations) is UT 2010 Nov. 4.1908, close to the moment of the *EPOXI* encounter which occurred 9.4 hr later. Our observations cover the epochs immediately before (37.2–29.5 hr and 13.4–5.8 hr) and after (10.4–18.3 hr) the flyby, while the moment of the encounter could not be covered because of the geographic longitude of the telescope. We observed HCN also one night earlier, on UT 2010 Nov. 2.06–2.37 (60.7–53.1 hr before the flyby), but excluded these spectra from the analysis because no counterpart spectra of CH₃OH were taken; nonetheless, we refer to these data on two occasions. At the epoch of observations the helio- and geocentric distances were 1.0631 and 0.1546 AU, respectively, and the geocentric phase angle was 58.82°. We consider these parameters as valid for the entire time series given that the changes in geometry were very small.

The two molecules were observed simultaneously with the Eight Mixer Receiver (EMIR): HCN at 265.9 GHz (E3 band) and CH₃OH at 157.2 GHz (E1 band). EMIR is a state-of-the-art sideband-separating dual-polarization instrument having a typical receiver temperature of 85 K in E3 and 50 K in E1. Spectral decomposition was performed simultaneously by the Versatile Spectrometer Array (VESPA) and the Wideband Line Multiple Autocorrelator (WILMA). For the analysis we chose the highest-resolution data from VESPA. The sections connected to E3 have 39.1-kHz spectral-channel spacing (resolution $R = 7 \times 10^6$) and 36.0-MHz bandwidth (921 spectral channels per polarization) and the sections connected to E1 provide 78.1-kHz spacing (resolution $R = 2 \times 10^6$) and 71.6-MHz bandwidth (917 spectral channels per polarization). In each band the two polarization channels were aligned to better than 2'' on the sky, which we concluded from frequent pointing calibrations on compact continuum sources (see further). Table 1 summarizes the transition and telescopic constants relevant to this work.

All the observations were obtained in *position-switching* mode, in which the whole antenna moves between the source position (ON) and a sky reference position (OFF). The offset between the two was 15' in azimuth, which secures OFF to be free (for all practical purposes) of cometary contribution (Drahus et al. 2010), and is still sufficiently close to ON to serve as a good reference giving relatively flat baselines. The integration times at ON and OFF were equal to 15 sec, which was chosen based on established instrumental and atmospheric characteristic timescales. We consistently used 24 ON–OFF pairs per spectrum, giving the total integration time at ON equal to 6 min, the total ON+OFF integration time of 12 min, and the effective observation time of ~ 15 min per spectrum (which includes all the overheads). Cometary observations were taken in approximately 1-hr blocks of 4 spectra, except for the three cases when we took 3 spectra per block. Each spectrum in a comet block has its own chopper-wheel calibration (Ulich & Haas 1976; Kramer 1997) which was used to automatically scale the signal in terms of antenna temperature; it was further converted to the main-beam brightness temperature T_{mB} scale using the main-beam

efficiency (Table 1). For the purpose of the present work we averaged the spectra within the blocks and altogether from the two polarization channels, to improve the signal-to-noise ratio. We used statistical weights inversely proportional to the square of the system temperature, which is a good proxy of noise when the integration time and spectral channels are the same for all the input spectra. We obtained the total of 21 such spectra for each molecule, 7 per night.

The blocks were preceded by measurements of pointing (and less frequently focus) corrections on nearby compact continuum sources, and snapshot spectral observations on nearby molecular line standards. The RMS pointing consistency was typically at the level of $2''$ in each axis, while the gain fluctuations rarely exceeded 10%. The control system of the 30-m telescope calculates the positions of comets in real time, assuming Keplerian orbits. We used the osculating elements obtained for the dates of observations with the JPL *Horizons* system¹ (Giorgini et al. 1997). The relative radial-velocity scale was obtained for each line from the absolute frequency scale through the classical Doppler law; zero velocity corresponds to the transition rest frequency, negative velocities to higher frequencies (blueshift) and positive velocities to lower frequencies (redshift). Topocentric Doppler corrections were applied automatically in real time.

The spectral baseline was calculated for each spectrum and separately for each of the observed CH₃OH lines. We used a linear fit in the interval between -10 and -3 km s⁻¹ and between $+3$ and $+10$ km s⁻¹, except for the close group of three CH₃OH lines (Fig. 1) for which a common baseline was calculated; in this case the baseline intervals were taken with respect to the outer lines. We used only full bins with native widths inside these intervals, however, bad channels, with signal exceeding a 3σ limit, were iteratively rejected. Then the signal scatter about the baseline was used to calculate noise RMS in the channels and the baseline was subtracted (cf. Paper I). Finally, each spectrum was rebinned to the standard velocity-resolution of 0.15 km s⁻¹ ($R = 2 \times 10^6$), very close to the native resolution of CH₃OH, and the signal error was propagated to the new channels. Such rebinned block-averaged spectra have practically independent channels – both in time and across the bandwidth.

We also additionally averaged the spectra in two different ways to further improve the signal-to-noise ratio: (i) for CH₃OH we calculated a time series of mean line profiles, obtained from all the 5 lines, and (ii) for both molecules we calculated their mean profiles (Figs. 1 and 2) upon averaging the spectra in the two time series. We used weights inversely proportional to the square of the signal error in the spectral channels. The former approach provides no information about line-to-line behavior but minimizes the noise in the time series and enables us to better analyze temporal variations. The latter gives no information about temporal behavior but minimizes the noise across the bandwidth and is naturally useful to derive “average” characteristics of the comet. Note that the result of approach (i) may be difficult to interpret when different lines of the same molecule have different shapes. This can happen when, for example, the predominant formation regions are different for the observed lines and the gas kinematics varies strongly across the coma

¹<http://ssd.jpl.nasa.gov/?horizons>

(Drahus et al. 2012). In our data, however, all the 5 lines display practically the same average shapes (Fig. 1), and hence we assume that they are also the same in each individual spectrum (this is difficult to verify given the much higher noise in the individual spectra). In this way, using the result of approach (ii) we validated approach (i).

The line profiles were parameterized in terms of the area $\int T_{\text{mB}} dv$ and median velocity v_0 . The parameters were derived from the interval between -1.75 and $+1.75$ km s $^{-1}$ centered at the zero velocity. Their errors were estimated from 500 simulations following our Monte Carlo approach, which we used to propagate the signal noise and also the uncertainty from imperfect pointing whenever relevant (see Paper I for details). As the errors we took the RMS deviations from the measured values, calculated for the positive and negative sides separately.

We interpret the observations with the aid of three basic physical quantities characterizing cometary gas: rotational temperature T_{rot} , production rate Q , and median radial (i.e. line-of-sight) flow velocity-component v_{rad} . These quantities were derived from the line parameters using the simple model briefly explained in Appendix A and fed with the constants from Table 1. It is important to realize that the absolute values of these quantities are uncertain due to several simplifying assumptions in this approach. Nevertheless, while we provide these absolute values, we focus on their temporal variations, which are affected to a much lesser extent (cf. the discussion in Drahus et al. 2010, where essentially the same approach was used). The errors were consistently derived from the simulated spectra as outlined above, except for the errors on T_{rot} (further discussed in Section 3). In the next sections we analyze these quantities and also the complete line profiles.

3. Rotational Temperature

We applied the *rotational diagram* technique (see Appendix A; also e.g. Bockelée-Morvan et al. 1994) to our CH $_3$ OH time series to determine the rotational temperature T_{rot} and its temporal variation. Selected examples of the rotational diagrams are presented in Fig. 3. Unlike any other uncertainties presented in this work, the errors on T_{rot} were derived not directly from the simulated set of spectra (cf. Section 2), but indirectly, upon propagating the RMS deviations of the slopes of rotational diagrams resulting from these simulations. That is because some of the simulations corresponding to the two flattest rotational diagrams (i.e. implying the highest T_{rot}) from spectra #1 and #8, yield marginally positive slopes and consequently non-physical temperatures. Nevertheless, the temperature limits resulting from the slope RMS are within the physical regime in all cases.

According to Biver et al. (2002a), the observed group of transitions at 157.2 GHz yields a rotational temperature very close to the kinetic temperature of the inner coma. The two temperatures are strictly equal in *Local Thermodynamic Equilibrium* (LTE), in which the energy levels are populated according to the Boltzmann distribution, and the resulting rotational diagrams are linear. Indeed, the majority of our rotational diagrams are indistinguishable, within the error bars,

from being linear, although in some cases we observe strong non-linearities or accidental deviations. While we cannot exclude instrumental effects (e.g. such as imperfect removal of the baselines) in the spectra behind these problematic diagrams, the possibility of large deviations from the Boltzmann energy-level distributions at these particular rotation phases cannot be ruled out at this stage.

The variability profile is presented in Fig. 4. We see large-amplitude variations which seem to generally follow the rotation-modulated production rate (see further Fig. 8 and the discussion in Section 4.1) although the correlation is not strict. While, again, occasional instrumental effects might have affected this trend, it seems extremely unlikely that the entire variability is an artifact. Instead, we believe that the variations are physical and their correlation with the production rate is real (Fig. 5) but additional fluctuations in the rotational temperature are superimposed on the regular trend. It is interesting to note, that although a positive correlation of these two quantities has been predicted by theory (e.g. Combi et al. 2004), only the correlations in long-term trends, primarily controlled by changing heliocentric distance, have been reported for individual objects to date (e.g. Biver et al. 2002a). Our result confirms that the rotational temperature is positively correlated with the production rate in a single object also when the received solar energy flux remains constant.

We also calculated a rotational diagram for the mean spectrum from Fig. 1. The diagram, presented in Fig. 6, is consistent with the temperature of 47 ± 2 K. While this value is some 30 K lower than the rotational temperatures from IR spectroscopy (Mumma et al. 2011; Dello Russo et al. 2011), the latter sampled a much smaller volume surrounding the nucleus, where the gas has presumably the highest temperature (e.g. Combi et al. 2004), and hence this difference should be expected and in fact was often noticed in the past (e.g. Drahus et al. 2010). It is important to realize that the gas sampled by our beam was presumably highly non-isothermal, both in time (see above) and across the coma (e.g. Combi et al. 2004), even if it locally satisfied LTE. Moreover, we cannot exclude that non-thermal processes significantly contributed to the overall excitation scheme, especially in the outer part of the sampled coma. Consequently, interpretation of the rotational temperature in such an environment is highly problematic, and some of these problems are discussed by Drahus et al. (2012).

4. Sources of HCN and CH₃OH

4.1. Average Production Rates and Temporal Variability

Both the average and the instantaneous production rates Q were derived assuming gas expansion velocity $v_{\text{gas}} = 0.8 \text{ km s}^{-1}$ and using the average rotational temperature $T_{\text{rot}} = 47 \text{ K}$ (Section 3). At this point we refrain from using the instantaneous T_{rot} for the calculation of the instantaneous Q , because of the relatively large errors on the individual temperatures (especially on the highest ones), the uncertain reason(s) for the occasional non-linearities of the rotational diagrams, and some uncertainty as to the cause(s) of the observed variability (cf. Section 3). In

Fig. 7 we show how the derived production rates depend on the adopted rotational temperature, and our assumptions and method are briefly summarized in Appendix A.

The derived average absolute production rates are 2.10×10^{26} molec s⁻¹ for CH₃OH and 1.25×10^{25} molec s⁻¹ for HCN. The production-rate ratio is about 17, which is the most typical value found in comets from millimeter spectroscopy (Biver et al. 2002b), but is somewhat higher than the values obtained for 103P in the infrared: ~ 10 (Mumma et al. 2011) and ~ 4.5 (Dello Russo et al. 2011). This inconsistency should again be no surprise, though, given all the differences in data acquisition and modeling, and also the natural variability of this comet, as even the two IR measurements from the same instrument give significantly different production-rate ratios.

We observe well-defined variation in the instantaneous production rates of both molecules (Fig. 8), which we previously noticed in HCN and connected with the rotation of the nucleus (Paper I). The two time series correlate remarkably well although the amplitudes are different, reaching a factor of 5 for HCN and a factor of 2 for CH₃OH.

The measured amplitude can differ from the real one if some of our model assumptions (Appendix A) are strongly violated, in particular (*i*) the negligible optical depth, (*ii*) the constant rotational temperature, or (*iii*) the outgassing properties.

A non-negligible optical depth would lead to an underestimation of the production rates, most significant for the brightest lines. Consequently, the amplitude of the brighter HCN would be reduced compared to the fainter CH₃OH, and since we observe otherwise, the real amplitude difference would have to be higher than measured. Nevertheless, the optical depth is completely negligible in our data, which is best evidenced by the hyperfine splitting of the HCN $J(3-2)$ line (Fig. 2). We make use of the fact, that the relative intensities of the hyperfine line components in a single molecule are established by fundamental physics and do not depend on the excitation conditions or mechanisms (Bockelée-Morvan et al. 1984). Consequently, if the component ratio measured in a molecular environment is equal to the theoretical value for a single molecule, it implies that these components are optically thin. Taking advantage of the exceptionally high signal-to-noise ratio in the average spectrum of HCN, we can easily distinguish the $F = 3 - 3$ hyperfine component and measure its area separately from the blend of the remaining components. We find the component ratio equal to 24^{+5}_{-4} which is in excellent agreement with the ratio of 26.0 predicted by theory (cf. Cologne Database for Molecular Spectroscopy²; Müller et al. 2005). This means that even the brightest region of the line, which is always first to saturate, is practically free of self-absorption. For this reason, we can also immediately conclude that the fainter lines of CH₃OH must be optically-thin as well.

Since the production rates were derived using the constant rotational temperature, they can be naturally affected by the measured temperature variations (Section 3). From the theoretical relation between these two quantities in Fig. 7 we see that the derived production rate depends on

²<http://www.astro.uni-koeln.de/cdms>

the temperature more strongly for CH₃OH than for HCN. This implies that the variations of the line area could not have been produced primarily by the varying temperature instead of the production rate, because the amplitude would be higher in CH₃OH than in HCN. Consequently, it must be a real variability of the production rate generating physical changes in the rotational temperature rather than the temperature variations modulating our derived production rates. However, the latter effect must also be present to some extent. Bearing in mind the suspected positive correlation of these quantities in our data (Fig. 5), we expect that the derived production-rate maxima are somewhat underestimated and the minima overestimated, although this reasoning is limited to $T_{\text{rot}} > 26$ K for which both functions in Fig. 7 monotonically increase (a lower T_{rot} was measured in only one data point, spectrum #14, and is equal to 19 K). Consequently, the observed amplitudes can be lower compared to the real ones, and since the effect is stronger for CH₃OH than for HCN, it can explain, at least to some degree, the different amplitudes measured in our data.

In the above discussion we assumed that the temperature variation is the same in HCN and CH₃OH. If, instead, the (unmeasured) characteristic temperature applicable to our HCN data varied more strongly, e.g. due to the smaller beam size (Table 1), the range of the production-rate offsets from Fig. 7 could even exceed the range for CH₃OH. This would imply that the real production-rate amplitudes differed more than inferred from our data, because HCN would be attenuated more strongly than CH₃OH. On the other hand, this scenario still cannot explain the derived production-rate variations as artifacts caused by the varying temperature (even though correctly implying the measured amplitude relation), because in such a case the two quantities would be negatively correlated while the determined correlation is evidently positive. While the situation can be, in principle, even more complex if, e.g. the two variability profiles of T_{rot} were totally different, we rather believe that the beam-size effect is of secondary importance in this respect – and hence the temperature in the data of both molecules is comparable, as we cannot identify other effects that could differentiate it significantly.

However, the different beam sizes can also affect the derived production rates in other ways, especially when the outgassing properties assumed in the model (Appendix A) are strongly violated. In fact, the outgassing of 103P is by no means in steady-state and isotropic, but rather dominated by rotating jets and icy grains periodically injected into the coma (see the next sections and references therein). In such a case, the observed amplitude can be smaller than the real one, by a factor which depends on the sublimation-time dispersion of the molecules contributing to a single spectrum (Drahus et al. 2010). In this way, the lower amplitude of CH₃OH seems to be naturally explained, given the larger beam size which effectively “sees” the molecules from a broader range of nucleus rotation phases compared to the smaller beam of HCN (Table 1). But this simple reasoning fails to explain the remarkable temporal correlation of both variability profiles, and also the fact that the maxima and minima look rather flat. Consequently, the timescale of variability appears sufficiently long compared to the integration and beam-escape times, to ensure that the outgassing properties are rather “frozen” on spatial and temporal scales characteristic of the CH₃OH and HCN data (Table 1). Steady-state is hence well-realized from a practical point of view, and both

production-rate profiles closely follow the instantaneous activity of the comet. (The two profiles are still deformed by the outgassing anisotropy, but both in a similar way.) This may indicate that the two diurnal amplitudes were indeed different. However, even if they were the same, the different beam sizes would still differentiate them in the same way as observed if, for example, the minimum level was produced by a constant background with uniform brightness distribution, i.e. if the central source of outgassing, assumed in the model, is not well satisfied.

Last but not least, we note that the errors of telescope pointing can also affect the derived production-rate profiles. Since the effect is negatively-correlated with the beam size, it affects HCN more strongly than CH_3OH , but in the same sense, and therefore it is consistent with their seeming temporal correlation and the relation of their amplitudes. However, given that the pointing corrections were always determined between the consecutive points in the time series, this effect is practically incapable of generating entire trends, introducing only small random deviations, and also its expected magnitude is rather small which is reflected by the derived error bars.

In order to fully understand the characteristics of the two production-rate profiles, we need to take into account the velocity information naturally contained in the lineshapes. Figure 9 shows the variability of the median radial gas-flow velocity v_{rad} . The behavior is also well-defined and consistent with the rotational periodicity of the nucleus. We see that the line-of-sight kinematics were noticeably different for the two molecules, in particular, HCN drifts towards deeply blueshifted velocities around the phases of maximum activity, while the velocities of CH_3OH change less. In Fig. 10 we show examples of the individual lineshapes. A close-up look reveals that HCN has a strong blueshifted component in the active phases, while CH_3OH looks symmetric with two distinct peaks. The difference vanishes at the transition and quiescent phases, when the lineshapes look remarkably similar to each other – featuring two symmetric peaks which resemble the lineshape of CH_3OH in the active phases (although the redshifted peak occasionally dominates both lines). The implication of these differences is that the sources of the two molecules must have differed in some way. We further explore this inference in the next section.

4.2. Interpretation of the Lineshapes

4.2.1. Basics of Lineshape Interpretation

Since the characteristic gas-flow velocity in comets 1 AU from the Sun is $\sim 1 \text{ km s}^{-1}$ (Combi et al. 2004), our spectra are fully “velocity-resolved” given the spectral resolution is 0.15 km s^{-1} (Section 2). The lineshapes in such spectra are primarily controlled by the Doppler effect. Other effects, including optical depth and hyperfine structure, can also theoretically influence the lineshapes but are negligible in our data. The velocity-calibrated spectra can be hence identified as histograms, showing how the observed molecules are distributed in radial velocity, weighted by the profiles of the beam sensitivity and the *emission coefficient* per molecule (the latter being a function of the excitation conditions in different regions of the coma).

This distribution depends on the directions in which the molecules travel: molecules traveling along the line of sight are either maximally redshifted or blueshifted, while molecules traveling normal to the line of sight are observed at their rest frequencies. If the molecules are ejected isotropically, then the emission line features two peaks symmetrically located about 0 km s^{-1} , with radial velocities equal to the positive and negative values of the gas-flow velocity (see model examples in Fig. 11). This is because most molecules in the beam travel either towards or away from the observer along the line of sight. Molecules traveling perpendicular to the line of sight leave the beam fastest producing a central minimum in the line profile. Moreover, real gas always has a “thermal” velocity component which blurs the lineshape. This effect is of secondary importance, though. For example, the thermal speed of CH_3OH at 47 K (Section 3) is only 0.2 km s^{-1} , small compared to the bulk gas-flow velocity of $\sim 1 \text{ km s}^{-1}$.

The travel directions of the molecules, at least in the inner coma, can be identified with the directions in which they sublimated, and therefore in the discussion below we directly link the observed spectral features with the characteristics of the 103P’s outgassing. At this stage we only aim at interpreting the most obvious spectral features and only in a qualitative manner. A more in-depth analysis requires a detailed lineshape modeling (cf. Drahus 2009), which is presently in preparation.

4.2.2. Evolution of the Lineshapes

The evolution of the lineshapes can be grouped in three distinct ranges of the nucleus rotation phase:

- Phases 0.4–0.5 (spectra #1 and #20–21): the *redshifted jet*.

The line profiles of CH_3OH and HCN look very similar. They feature a well-defined redshifted peak at about $+0.3 \text{ km s}^{-1}$, which we identify with a *redshifted jet* directed away from the Earth (as projected onto the line of sight). The gas in the jet was abundant in both CH_3OH and HCN , and must originate from a vent (or a group of vents) on the nucleus, which was active only in these particular rotation phases.

- Phases 0.5–1.0 (spectra #2–7, #8–11, and #21): the *blueshifted jet*.

Essentially half of the rotation cycle, between phases 0.5 and 1.0, is dominated by the phenomena associated with the appearance of the *blueshifted jet*.

- The first signatures are visible in HCN around phase 0.5. The HCN lineshape starts showing a blueshifted peak, which is visible simultaneously with the redshifted peak from the earlier jet (spectrum #21, and between #1 and #2). At the same time, CH_3OH still shows only the redshifted peak.

- Around phase 0.55 (spectrum #2) the blueshifted peak starts dominating the HCN spectrum, while CH₃OH becomes symmetric with two distinct peaks.
- Between phases 0.6 and 0.8 (spectra #3–5 and #8–9) both lines rapidly brighten, while their profiles remain unchanged, starkly differing from each other: HCN has a single, strong blueshifted peak near -0.6 km s^{-1} , and CH₃OH has two symmetric peaks, one about -0.55 km s^{-1} and the other one close to $+0.4 \text{ km s}^{-1}$.
- After reaching the maximum brightness around phase 0.8, the two lines start fading until about phase 1.0 (spectra #6–7 and #10–11). The transition between the brightening and fading phases is associated with a dramatic change in the HCN line profile, which starts showing two symmetric peaks. At the same time, the line profile of CH₃OH remains the same as in the brightening phase, and so both lines fade looking strikingly similar to each other.

The lineshapes showing the strong blueshifted peak are naturally identified with a *blueshifted jet* directed towards the Earth (as projected onto the line of sight). On the other hand, the symmetric double-peak lineshapes can be easiest interpreted as created by an isotropic source. While it is difficult to expect the jet-dominated nucleus to directly act as such a source, it is easy to imagine that this role was played by isothermal icy grains moving at negligible own velocities (compared to the velocity of gas). Indeed, the images from the *EPOXI* flyby show an unexpected abundance of large icy grains close to the nucleus, up to 10–20 cm in radius, most of which move at velocities $< 0.5 \text{ m s}^{-1}$ and none faster than 2 m s^{-1} (A’Hearn et al. 2011). Also the Arecibo radar detected centimeter to decimeter grains with velocities of the order of few to tens of meters per second (Harmon et al. 2011). These velocities are negligible compared to the gas velocity ($\sim 1 \text{ km s}^{-1}$ at this heliocentric distance; cf. Combi et al. 2004), and it is most natural to assume that the grains were isothermal, which altogether makes them excellent candidates to explain the symmetric double-peak line profiles.

Bearing the above in mind, we interpret the overall behavior of the lineshapes between the rotation phases 0.5 and 1.0 as being controlled by the *blueshifted jet* dragging fair amounts of icy grains. The jet must originate from a vent (or a group of vents) on the nucleus, which was active only in these particular rotation phases. The outgassing from the vent was directed towards the Earth, and was rich in HCN but not in CH₃OH. In contrast, the excavated icy grains sublimated isotropically and carried abundant HCN and CH₃OH in proportions comparable to the gas in the *redshifted jet* observed at the earlier phases. The composition of the grains appears then dramatically different from the composition of the gas in the *blueshifted jet* which carried them away from the nucleus. Consequently, in these rotation phases, the observed HCN sublimated both from the grains and from the active vent, while the observed CH₃OH sublimated only from the grains.

At the onset of the *blueshifted jet*, the observed HCN coma was dominated by the gas in this jet, and therefore the HCN line displays the blueshifted peak. However, at the same time, the observed coma of CH₃OH was dominated by the gas sublimating from the first grains, and

therefore CH_3OH started brightening with some delay, and the lineshape is symmetric with two peaks. With time, the grains cumulated near the nucleus, and also the outgassing rate from the vent increased (excavating even more grains). This corresponds to the rapid brightening of both lines, and explains why their profiles differ so much. CH_3OH , sublimating only from the grains (isotropically), brightened double-peaked, while HCN, produced additionally by the active vent (anisotropically), brightened strongly blueshifted. At some point, the sublimation from the vent declined, but the grains emitted earlier persisted for a little while, and that is when the lineshapes of CH_3OH and HCN became strikingly similar to each other, showing two symmetric peaks. While the grains continued losing their total cross-section and (perhaps negligible) moving away from the beam center, the lines were fading but their shapes remained unchanged. Indeed, A’Hearn et al. (2011) suggested that the total cross-section of the grains was controlled by the finest particles, and hence the total sublimation area of the grains must have quickly declined when the smallest ones totally changed into gas.

- Phases 0.0–0.4 (spectra #12–19): quiescent rotation phases.

The CH_3OH and HCN lines look very much alike. In most of the spectra, they show symmetric double-peak profiles, which we have earlier identified with isothermal icy grains. The brightness of the lines stabilized at some minimum level, i.e. neither strongly declined with the increasing rotation phase, nor rose up with the increasing count of the rotation cycles. This leads us to the conclusion, that the total sublimating area of these grains was fairly constant on a rotation-cycle timescale. We suppose that the grains were large and slow – hence could survive in our beam for multiple rotation cycles, and emitted at low rates – hence the contribution from a single cycle was negligible. If true, the constant background produced by these grains was present at all rotation phases but it was difficult to identify when other features dominated the spectra. Taking this into account, it is understandable that we cannot identify the rotation phases at which these large grains were emitted, although it is natural to suspect the *blueshifted jet*, which we have identified as the main supplier of the smaller grains.

4.2.3. Additional Remarks

It is important to emphasize, that because of the very short gas escape time from the beam (Table 1), the observed line profiles reacted almost instantly to the changes in the activities of the nucleus itself and near-nucleus grains (cf. Section 4.1). For this reason, the overall above scenario also naturally explains the remarkable production-rate correlation in CH_3OH and HCN (Fig. 8). Other scenarios, which are discussed in Section 4.1, cannot be accepted because they fail to explain the observed differences in the lineshapes. Specifically:

- The varying optical depth can, in principle, produce temporal changes in the line profiles, but we concluded that both lines were optically thin.
- The variations in the rotational temperature are rather difficult to connect with the lineshapes.

- Potential problems with pointing are unlikely to generate systematic trends or, for the still stronger reason, periodic trends.
- In the suspected situation in which the production-rate amplitudes are differentiated by the different beam sizes (due to background) but the sources of CH₃OH and HCN in the comet are the same, CH₃OH would also display a blueshifted component in the phases dominated by the *blueshifted jet* (albeit somewhat fainter than in HCN) but we do not see it in our data. Moreover, we concluded that the grains must have been localized very close to the nucleus, hence effectively acting as a central source in our data.
- We also note that the line profiles of CH₃OH and HCN naturally differ due to the presence of hyperfine splitting, but this difference is “static” (for optically-thin lines; cf. Section 4.1), and rather small (Fig. 11).

While we cannot exclude that some of the above mechanisms contributed, to some extent, to the observed differences between the lines, clearly none of them can be an alternative to the postulated difference in the sources of CH₃OH and HCN. Nevertheless, the proposed interpretation of the lineshapes is not unique, and other, perhaps more complicated scenarios, may explain the observed behavior equally well or even better.

It is interesting to note that, at the comet’s phase angle $\sim 60^\circ$ (Section 2), the Sunward direction projects as blueshifted and most of the illuminated part of the nucleus would emit material in the blueshifted directions. However, a smaller but still substantial fraction of the illuminated part would emit material in the redshifted directions. For this reason, it is entirely possible that both the vent producing the *blueshifted jet* and the vent producing the *redshifted jet* were illuminated while being active. However, we suppose that the *redshifted jet* originate from a vent close to the region of the polar night, which was illuminated during only a short fraction of the rotation cycle. This would naturally explain its short duration and opposite radial velocity-component compared to the *blueshifted jet*. Supposing that the gas-flow velocity was comparable in the two jets, perhaps close to 0.8 km s^{-1} (Appendix A), we take into account the difference in velocity offsets of the line peaks ($+0.3 \text{ km s}^{-1}$ for the *redshifted jet* vs. -0.6 km s^{-1} for the *blueshifted jet*), and conclude different significance of the projection effect – implying that the *blueshifted jet* was emitted in a direction close to the line of sight, while the *redshifted jet* was relatively closer to the sky plane. The role of the icy grains in the *redshifted jet* is difficult to evaluate because the *blueshifted jet* appeared immediately after. We also note, that the fact that the two seemingly different jets appeared at consecutive rotation phases, makes them hard to distinguish in the time series of the total production rate (Fig. 8). However, expanding in the opposite directions (as projected onto the line of sight), they clearly manifest themselves as separate features in the velocity-resolved line profiles.

4.2.4. Differences Between Rotation Cycles

The above simple scenario presents a coherent explanation of the primary spectral characteristics of both lines. Small deviations from this scenario naturally exist, and can be attributed to the weaker outgassing sources observed by *EPOXI* (A’Hearn et al. 2011). When attempting to identify the smallest inconsistencies, one should also keep in mind the limited signal-to-noise ratio and baseline reliability of these data, as well as the limited pointing accuracy of the telescope. Finally, the adopted catalog constants might be possibly held responsible for small inconsistencies, such as the small systematic redshift of CH₃OH compared to HCN, independent of the lineshape (Fig. 9).

While we will not investigate these issues any further, we spell out three deviations from the above scenario which are well-defined, and which may be possibly associated with the excitation of the nucleus rotation state (cf. Paper I; also A’Hearn et al. 2011; Knight & Schleicher 2011; Samarasinha et al. 2011; Waniak et al. 2011).

- The phases 0.1–0.2 (spectra #13–14) on UT Nov. 4 (*Cycle B*) show, that the lines of CH₃OH and HCN are consistently dominated by the redshifted peak, resembling the lineshapes previously identified with the *redshifted jet* at phases 0.4–0.5 (Section 4.2.2). However, on UT Nov. 5 (*Cycle C*) the spectra at phases 0.1–0.2 (#16–17) look typical of the quiescent phases, i.e. show two symmetric peaks and are generally fainter than on UT Nov. 4 (*Cycle B*).

We suppose that the redshifted lineshapes, appearing at the two separate phase ranges, might have been produced by the same *redshifted jet* identified earlier. Because of the excitation of 103P’s rotation and the likely circum-polar origin of the *redshifted jet* (Section 4.2.2), the parent vent might have been activated by insolation at phases 0.4–0.5 during *Cycle C*, but earlier – at phases 0.1–0.2 – during *Cycle B*. This interpretation is consistent with the fact that in both cases the lineshapes of CH₃OH and HCN look very similar (unlike in the phases dominated by the *blueshifted jet*) and is additionally confirmed by the HCN data from UT Nov. 2 (see further in this paragraph).

- The excitation of the rotation state is also likely responsible for the fact that at the rotation phase 0.82 of *Cycle C* (spectrum #6 obtained on UT Nov. 3) the lineshapes are more evolved than at exactly the same phase of *Cycle A* (spectrum #9 obtained on UT Nov. 4). Given the remarkable coincidence in phase of the *redshifted jet* observed during two consecutive *Cycles C* (Section 4.2.2), the above inconsistency cannot be removed by simply adjusting the 18.33-hr rotation period.
- The spectra of HCN taken on UT Nov. 2 (formally excluded from the analysis because no counterpart spectra of CH₃OH were taken), covering phases 0.2–0.6 of *Cycle B*, show that the *redshifted* and *blueshifted jets* appeared at relatively earlier rotation phases than in *Cycle C* observed on UT Nov. 3 and 5. This behavior is consistent with the rotational production-rate profiles from a much bigger dataset presented in Paper I.

On UT Nov. 2 the *redshifted jet* is visible at phases 0.2–0.25, which agrees remarkably well with the short *Cycle B* data from UT Nov. 4 (covering phases 0.05–0.2), in which we have identified this jet at phases 0.1–0.2 (see earlier in this paragraph). Combining these two pieces of *Cycle B* data we conclude that the *redshifted jet* was present at phases 0.1–0.25, with a subtle local minimum at phase 0.2.

Moreover, in *Cycle B* the blueshifted peak looks fainter than in *Cycles C* and *A*, which may indicate that the *blueshifted jet* was physically weaker (e.g. due to different insolation), although other explanations may be possible as well (e.g. a different projection effect). Whatever the cause, in *Cycle B* the *blueshifted jet* triggers a comparable amount of icy grains as in *Cycles C* and *A* and, consequently, in the phases of maximum brightness the HCN line features a symmetric double-peak profile.

Summarizing, the observed deviations from the simple scenario presented in Section 4.2.2 can be plausibly associated with the excitation of 103P’s rotation state. They also agree remarkably well with the *three-cycle* scenario which we introduced in Paper I to approximate repeatability in any rotation-modulated data of this comet.

5. Discussion

The velocity-resolved spectral time series of CH₃OH and HCN reveal a complex outgassing portrait of 103P. We identify outgassing in the form of at least two jets – the *redshifted jet* and the *blueshifted jet* – expanding in the opposite directions (as projected onto the line of sight), and having seemingly different compositions. The *blueshifted jet* appears as a strong source of HCN gas and of icy grains, but not of CH₃OH gas. The composition of the grains is, however, dramatically different from the composition of the gas in this jet, because, in addition to HCN, they also contain large amounts of CH₃OH. But the grains composition closely resembles the gas in the *redshifted jet*, which was rich in HCN and CH₃OH. Consequently, the origin of the observed CH₃OH and HCN can be summarized as follows:

- CH₃OH:
 - anisotropic sublimation from the active vent which produced the *redshifted jet*,
 - isotropic sublimation from the icy grains carried away primarily in the *blueshifted jet*, but not from the vent itself (at least not at any measurable level).
- HCN:
 - anisotropic sublimation from the active vent which produced the *redshifted jet*,
 - anisotropic sublimation from the active vent which produced the *blueshifted jet*,
 - isotropic sublimation from the icy grains carried away primarily in the *blueshifted jet*.

The properties of these two jets resemble very much the CN features observed around the same time in narrowband optical images (Knight & Schleicher 2011; Samarasingha et al. 2011; Waniak et al. 2011). In particular, the images of Waniak et al. (2011) – obtained nearly simultaneously with our IRAM 30-m data – are dominated by structures with low projected sky-plane velocities, hence expanding close the line-of-sight direction (the *slow CN feature*). We tentatively associate these features with our *blueshifted jet*, given the dominating role of the *blueshifted jet* in our data and also its strong Doppler shift. However, a small part of the dataset of Waniak et al. (2011) shows a much faster feature, expanding in the S–SW direction (the *fast CN feature*) probably not far from the sky plane. Interestingly, Knight & Schleicher (2011) and Samarasingha et al. (2011) report that the S–SW feature became first visible only in October. Consequently, we suppose that it is the same structure as our *redshifted jet*, having a relatively weak Doppler shift, and supposedly just emerging from the polar night.

We have earlier established (Paper I) that the variability of the HCN production rate was in phase with the brightness variation in CO₂ and H₂O observed by *EPOXI* (A’Hearn et al. 2011). Consequently, CH₃OH also correlates with all these molecules. But even though the variations of the four molecules were in phase, the spatially-resolved molecular observations from *EPOXI* revealed different reservoirs of CO₂ and H₂O, and our own observations show differences between HCN and CH₃OH. Interestingly, however, the variability amplitudes³ of HCN and CH₃OH, reaching a factor of 5 and a factor of 2, respectively, are the same as measured for CO₂ and H₂O. An intriguing hypothesis arises then, that perhaps HCN is spatially correlated in the nucleus with CO₂ and CH₃OH with H₂O. Consequently, we suppose that the *redshifted jet* (tentatively associated with the *fast CN feature*) was observed by *EPOXI* as the *water jet*, while the *blueshifted jet* (tentatively associated with the *slow CN feature*) was observed by the spacecraft as the *carbon dioxide jet*. Moreover, the *carbon dioxide jet* is a strong supplier of icy grains in the *EPOXI* data (A’Hearn et al. 2011) and the same is true for the *blueshifted jet* in our data.

At this stage it is difficult to accurately quantify how much gas originates directly at the nucleus and how much was produced from the grains in the coma. Nevertheless, taking into account that in about half of the HCN spectra, and in most of the CH₃OH ones, the lines have two symmetric peaks (which we associate with the grains), we can very crudely estimate that probably about half of the HCN molecules, and most of the CH₃OH ones, sublimated from the grains. This conclusion is in agreement with the statement of A’Hearn (2011) based on the *EPOXI* data. However, we also note that in *Cycle B* covered on UT Nov. 2 (just one *three-cycle* before the *EPOXI* flyby, which occurred at the middle of the next *Cycle B*), the *blueshifted jet*, which is the main supplier of the icy grains, appeared weaker than in *Cycles A* and *C*, but excavated a comparable amount of the

³Due to excitation of the rotation state the pattern of variability repeats best every three rotation cycles (Paper I; also A’Hearn et al. 2011). We observed the minimum and maximum levels during different rotation cycles but they correspond to the same *three-cycle* component (*Cycle C*). Nevertheless, due to the residual differences between the same *three-cycle* component observed at different times, the absolute amplitudes of HCN and CH₃OH should be interpreted with some caution.

grains. Consequently, at phase 0.5 of this cycle (corresponding to the moment of the encounter), the HCN spectra are totally dominated by the icy grains. This may indicate that *EPOXI* visited 103P when the grains were exceptionally abundant and hence the information inferred from the flyby may not represent the typical behavior of the comet.

It is now our ongoing effort to model the entire set of line profiles in a non-steady-state anisotropic fashion (cf. Drahus 2009), simultaneously with the image time series of CN (Waniak et al. 2011). We wish to take advantage of the fact that both types of data contain the velocity information in orthogonal dimensions and hence are fully complementary. The result will be used to constrain a 3D outgassing portrait and retrieve the source locations of CH_3OH and HCN, which will be readily comparable with the spatially-resolved observations of CO_2 and H_2O from *EPOXI*. Consequently, we will verify the postulated identities of the various features emerging from the different datasets, which are only hypothetical at this stage. We will also better understand the sublimation dependence on insolation, quantify the gas contribution from the icy grains, and obtain realistic, time-dependent absolute production rates and gas-flow velocities.

The compositional heterogeneity with respect to CO_2 and H_2O can be possibly explained by the different characteristic sublimation temperatures: 72 K and 152 K, respectively (Yamamoto 1985). This should compositionally decouple these molecules both in the protosolar environment (different locations of the *snowlines*) and also later, in the thermally-processed ices of Jupiter-family comets (Guilbert-Lepoutre & Jewitt 2011). In contrast, HCN and CH_3OH have practically the same sublimation temperatures, 95 K and 99 K, respectively (Yamamoto 1985), and therefore the observed heterogeneity may suggest that they underwent different condensation processes. Perhaps HCN can at least partly escape from water ice, while CH_3OH is fully incorporated in it – either in the form of clathrate-hydrates, or as trapped gas within the (amorphous) ice matrix (e.g. Prialnik et al. 2004). If true, it seems entirely possible that a part of 103P’s nucleus has been more heated in the past and therefore lost its volatiles except for water and the molecules incorporated in water ice (CH_3OH , HCN, ...), and that is where the *redshifted jet* originates from. At the same time, another part can be more primordial and dominated by free volatiles (CO_2 , HCN, ...) rather than H_2O and the water-bonded elements, and that is where the *blueshifted jet* is formed. However, water and the molecules incorporated in water ice are emitted from this part in the form of solid icy grains, and therefore we suppose that they also directly sublimate from this area, but at rates so much lower compared to the free volatiles that they remain undetected.

If this scenario is true, the nucleus of 103P might have been born as a body in which the molecules were uniformly mixed in a bulk sense. In that case we would expect that the *redshifted jet* was much stronger in the past, when the free volatiles dominated it completely as currently observed in the *blueshifted jet*. However, in the course of time the thermal evolution of the body reversed the jet strengths. It is suggestive that we currently observe the *blueshifted jet* on its way to completely lose the free volatiles and become compositionally similar to the evolved *redshifted jet*, but presumably much weaker. This process, if sufficiently fast, may be responsible for the significant decline in activity of 103P compared to the previous return (cf. Combi et al. 2011, albeit measured

through a proxy for water). Last but not least, given the above evolutionary constraints, it is more appropriate to characterize the *redshifted jet* as “HCN-depleted” rather than the *blueshifted jet* as “CH₃OH-depleted”, although from the observational point of view it seems counterintuitive at first glance.

Our results demonstrate the scientific potential of dense time series of velocity-resolved spectra taken at millimeter wavelengths. We found large-scale heterogeneity of 103P’s nucleus with respect to HCN and CH₃OH, which was not reported by two groups observing independently in the infrared. We suspect that the dense time series of Dello Russo et al. (2011) is too incomplete to show the compositional differences between different parts of the nucleus, as it covers only 17% of the rotation cycle in HCN (two exposures) overlapping with 28% coverage in CH₃OH (five exposures). The sparsely-sampled data of Mumma et al. (2011) may suffer likewise. Moreover, insight into the line-of-sight kinematics, naturally available for comets via millimeter spectroscopy, is still unreachable in IR. On the other hand, the IR observations are complementary to those in the millimeter wavelength regime by providing spatial profiles along the slit, which are more difficult to obtain using single-dish millimeter spectroscopy. Both groups observing 103P in the infrared report similar distributions of H₂O and CH₃OH, while HCN differed to some extent – the characteristics which our work fully supports.

6. Summary

We observed comet 103P/Hartley 2 using the 30-m IRAM telescope between UT 2010 Nov. 3.0 and 5.4. At a spectral resolution of 2×10^6 , velocity-resolved spectra of CH₃OH and HCN show strong variability of the production rate, median-radial velocity, detailed lineshape, and – in the case of CH₃OH – of the rotational temperature. We associate the observed variations with the properties of different regions of the nucleus successively exposed to sunlight over the course of its rotation. Our results can be summarized as follows:

1. We identify three distinct outgassing components in velocity-resolved spectral line data. There are two jets with opposite radial velocity-components (the *redshifted jet* and the *blueshifted jet*) and an isotropic component evidently produced by sublimation from near-nucleus icy grains. The latter are injected into the coma primarily through the *blueshifted jet*.
2. The nucleus of 103P is globally heterogeneous with respect to CH₃OH and HCN. Collimated flows of these two molecules are present in the *redshifted jet*, but only HCN flow is detected in the *blueshifted jet*. Both molecules are also detected in the icy grains in proportions comparable to those in the *redshifted jet*.
3. HCN is probably partly incorporated in water ice (either in the form of clathrate-hydrates, or as trapped gas within the amorphous ice matrix) but also exists unbonded to water, while CH₃OH is mostly or fully trapped.

4. The vent producing the *redshifted jet* appears thermally evolved (depleted in free volatiles). We suppose that it was located close to the region of the polar night, and tentatively link it with the *fast CN feature* (visible from the ground) and *water jet* (observed by *EPOXI*). The vent producing the *blueshifted jet* appears more primordial (rich in free volatiles), and we tentatively link it with the *slow CN feature* (visible from the ground) and *carbon dioxide jet* (observed by the spacecraft).
5. The variations in both molecules show small but obvious deviations from strict periodicity which are consistent with the *three-cycle* repeatability pattern. We interpret this as another indication of the excitation of the nucleus rotation state.
6. The rotational temperature varies strongly and is loosely correlated with the varying production rate.
7. The average rotational temperature is 47 K, and the average production rates are: 2.10×10^{26} molec s⁻¹ for CH₃OH and 1.25×10^{25} molec s⁻¹ for HCN. All three values are typical of comets.

The complete material used in this study is available in the paper’s *online version*. Figure 12 and Animation 1 show the full set of rotational diagrams, while Fig. 13 and Animation 2 show all the lineshapes.

We thank Steve Charnley and Karin Öberg for valuable discussions, and acknowledge support from NASA through a Planetary Astronomy Program grant to D. J.

Facilities: IRAM:30m (EMIR).

A. Derivation of Physical Quantities from Spectral Lines

The line was parameterized in terms of the area $\int T_{\text{mB}} dv$ integrated in the radial-velocity space, and median velocity v_0 (Section 2). Since the zero velocity corresponds to the optocenter of the hyperfine structure, the median line velocity can be immediately recognized as the median radial gas-flow velocity, $v_0 = v_{\text{rad}}$, assuming that (i) the sampled region of coma is optically thin at the observed frequencies. The line area can be converted to the production rate Q using a simple model, which additionally assumes (ii) Boltzmann distribution of the energy levels throughout the coma, (iii) volume density of the molecules inversely proportional to the square of the nucleocentric distance, i.e. negligible photodissociation losses, (iv) isotropic and constant in time ejection of the molecules from a central source, (v) constant in space and time bulk gas-flow velocity v_{gas} and temperature T (note that *thermal equilibrium* implies that the rotational temperature is equal to the kinetic temperature, therefore we simply refer to the gas temperature).

Under these assumptions the production rate Q can be easily obtained from $\int T_{\text{mB}} dv$ using a

simple formula (see Drahus 2009, for derivation):

$$Q = \frac{16\pi}{\sqrt{\pi \ln 2}} \frac{k}{hc^2} \frac{\nu_0}{A_{ul}} \frac{Z(T)}{g_u e^{-E_u/kT}} \frac{b\Delta}{D} v_{\text{gas}} \int T_{\text{mB}} dv \quad (\text{A1})$$

where k and h are the Boltzmann and Planck constants, respectively, and c is the speed of light; the transition from the upper rotational energy level u to the lower level l is parameterized by the rest frequency of the emitted photon ν_0 , Einstein coefficient for spontaneous emission A_{ul} , degeneracy of the upper state g_u , and the upper state energy E_u ; the partition function is $Z(T) = \sum_i g_i \exp(-E_i/kT)$; the telescope is characterized by the dish diameter D and a dimensionless parameter b connecting the beam FWHM with the dish diameter: $\text{FWHM} = b c / (D \nu_0)$; for IRAM 30 m we take $D = 30$ m and $b = 1.13$, the latter derived from the beam sizes given in the online documentation⁴; finally, Δ is the topocentric distance.

Equation (A1) immediately implies:

$$-E_u/T = \ln \left(\frac{\nu_0}{g_u A_{ul}} \int T_{\text{mB}} dv \right) + \text{const} \quad (\text{A2})$$

for different lines of the same molecule. It provides a convenient way of determining T from the slope of the linear relation between E_u and the logarithmic term, and is called the *rotational diagram* technique (cf. Bockelée-Morvan et al. 1994).

Our procedure was as follows: (i) we first used Eq. (A2) to obtain the temperature T from the areas of the 5 lines of CH₃OH, then (ii) we calculated the partition functions $Z(T)$ for this temperature, and finally, (iii) we substituted in Eq. (A1) the obtained T and $Z(T)$ and the assumed $v_{\text{gas}} = 0.8$ km s⁻¹ to convert the line areas $\int T_{\text{mB}} dv$ into the production rates Q . The molecular constants were taken from Table 1. For CH₃OH we converted the average line profiles, because from Eq. (A2) we knew the line ratios.

The partition function $Z(T)$ was linearly interpolated in a log-log space from the catalog values available for a range of temperatures. We used the Cologne Database for Molecular Spectroscopy⁵ (CDMS; see Müller et al. 2005) for HCN and the JPL Molecular Catalog⁶ (Pickett et al. 1998) for CH₃OH; the partition function information for methanol is not included in CDMS. While we investigate the behavior of the (rotational) temperature in time (Fig. 4), we calculated the production rates of both molecules (Fig. 8) using the constant temperature from the mean spectrum (Figs. 1 and 6), equal to 47 K. The actual adopted value is not very important for the presented results, because it simply scales the production rates of a given molecule by a constant factor and therefore only affects the molecule-to-molecule ratio. The role of the gas velocity is even less

⁴<http://www.iram.es/IRAMES/mainWiki/Iram30mEfficiencies>

⁵<http://www.astro.uni-koeln.de/cdms>

⁶<http://spec.jpl.nasa.gov>

important as it identically scales the production rates of both molecules and does not affect the rotational temperature in the framework of our simple model (Eqs. A1 and A2). This velocity can be, in principle, retrieved from the line profiles, but it is not a trivial task for jet-dominated activity (Drahus 2009). At this point we refrain from deriving it in the framework of the above isotropic model (although such an approach has been widely used in the past), adopting instead a common literature value $v_{\text{gas}} = 0.8 \text{ km s}^{-1}$ suggested for many comets around the same heliocentric distance and generally consistent with model predictions. The real issues can be caused by temporal variations of these quantities, such as the influence of the varying T_{rot} discussed in Section 4.1.

REFERENCES

- A’Hearn, M. F., 2011, EPSC Abstracts, 6, 316
- A’Hearn, M. F., et al., 2011, Science, 332, 1396
- Biver, N., et al., 2002a, EM&P, 90, 5
- Biver, N., et al., 2002b, EM&P, 90, 323
- Bockelée-Morvan, D., et al., 1984, A&A, 141, 411
- Bockelée-Morvan, D., Crovisier, J., Colom, P., Despois, D., 1994, A&A, 287, 647
- Combi, M. R., Harris, W. M., Smyth, W. H., 2004, in Comets II, eds. M. C. Festou, H. U. Keller, H. A. Weaver (Tucson: Univ. of Arizona Press), 523
- Combi, M. R.; Bertaux, J.-L., Quémerais, E.; Ferron, S.; Mäkinen, J. T. T., 2011, ApJ, 734, L6
- Dello Russo, N., et al., 2007, Nature, 448, 172
- Dello Russo, N., et al., 2011, ApJ, 734, L8
- Dones, L., Weissman, P. R., Levison, H. F., Duncan, M. J., 2004, in Comets II, eds. M. C. Festou, H. U. Keller, H. A. Weaver (Tucson: Univ. of Arizona Press), 153
- Drahus, M., 2009, *Microwave observations and modeling of the molecular coma in comets*, Ph. D. thesis (Univ. of Göttingen)
- Drahus, M., et al., 2010, A&A, 510, A55
- Drahus, M., et al., 2011, ApJ, 734, L4
- Drahus, M., et al., 2012, AJ, submitted
- Duncan, M., Levison, H., Dones, L., 2004, in Comets II, eds. M. C. Festou, H. U. Keller, H. A. Weaver (Tucson: Univ. of Arizona Press), 193

- Feaga, L. M., A’Hearn, M. F., Sunshine, J. M., Groussin, O., Farnham, T. L., 2007, *Icarus*, 191, 134
- Gibb, E. L., et al., 2007, *Icarus*, 188, 224
- Giorgini, J. D., et al., 1997, *BAAS*, 28, 1099
- Guilbert-Lepoutre, A., Jewitt, D., 2011, *ApJ*, 743, 31
- Harmon, J. K., Nolan, M. C., Howell, E. S., Giorgini, J. D., Taylor, P. A., 2011, *ApJ*, 734, L2
- Hartley, M., 1986, *IAUC* 4197
- Knight, M. M., Schleicher, D. G., 2011, *AJ*, 141, 183
- Kramer, C., 1997, *Calibration of spectral line data at the IRAM 30m radio telescope*, IRAM Report
- Levison, H. F., 1996, *ASPC*, 107, 173
- Levison, H. F., Duncan, M. J., Brasser, R., Kaufmann, D. E., 2010, *Science*, 329, 187
- Mumma, M. J., et al., 2011, *ApJ*, 734, L7
- Müller, H. S. P., Schlöder, F., Stutzki, J., Winnewisser, G., 2005, *J. Mol. Struct.*, 742, 215
- Pickett, H. M., et al., 1998, *J. Quant. Spec. Radiat. Transf.*, 60, 883
- Prialnik, D., Benkhoff, J., Podolak, M., 2004, in *Comets II*, eds. M. C. Festou, H. U. Keller, H. A. Weaver (Tucson: Univ. of Arizona Press), 359
- Rothman, L. S., et al., 2005, *J. Quant. Spec. Radiat. Transf.*, 96, 139
- Samarasinha, N. H., Mueller, B. E. A., A’Hearn, M. F., Farnham, T. L., Gersch, A., 2011, *ApJ*, 734, L3
- Ulich, B. L., Haas, R. W., 1976, *ApJS*, 30, 247
- Waniak, W., Borisov, G., Drahus, M., Bonev, T., 2011, *A&A*, submitted
- Weidenschilling, S. J., 1977, *MNRAS*, 180, 57
- Yamamoto, T., 1985, *A&A*, 142, 31

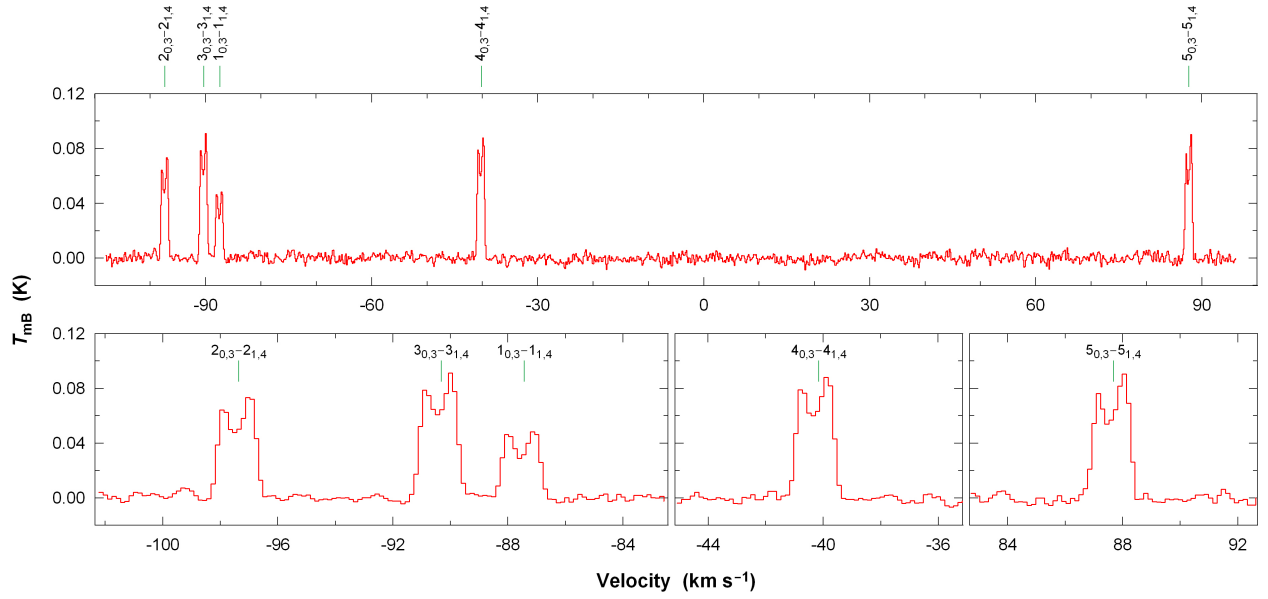


Fig. 1.— Mean spectrum of CH₃OH resulting from all the 21 spectra in our time series. The zero velocity corresponds to the rest frequency of 157.225 GHz. The transitions are labeled and the rest velocities are indicated by the short green vertical lines. The *top panel* shows the full spectrum whereas the *bottom panels* show close-up views of the line profiles.

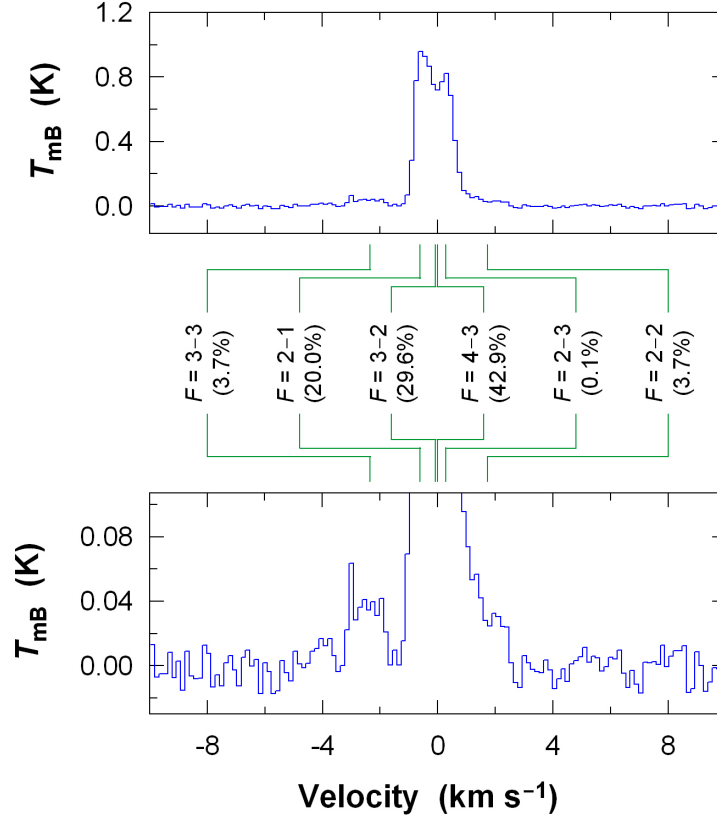


Fig. 2.— Mean spectrum of HCN $J(3-2)$ resulting from all the 21 spectra in our time series. The green lines indicate the velocities of the hyperfine components taken from the Cologne Database for Molecular Spectroscopy (Müller et al. 2005); they are labeled and their theoretical branching ratios are given in the brackets. The *top panel* shows the complete line whereas the *bottom panel* shows a close-up view of the baseline. It is evident that, in addition to the three strongest hyperfine components which build up the line, two faint components are also visible: one fully resolved at $-2.3545 \text{ km s}^{-1}$ ($F = 3 - 3$) and the other one in the red wing of the line at $+1.7394 \text{ km s}^{-1}$ ($F = 2 - 2$).

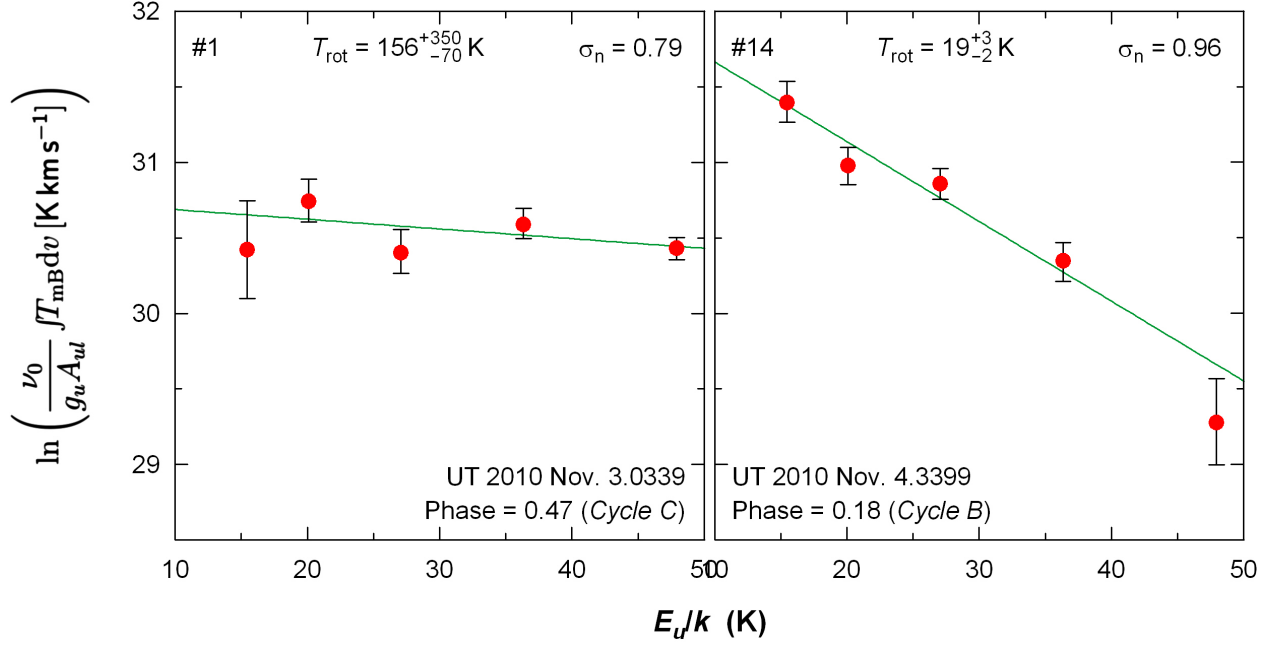


Fig. 3.— Individual rotational diagrams derived from the time series of CH_3OH , with weighted linear fits. The selected examples correspond to the maximum (*left*) and minimum (*right*) temperatures T_{rot} . The weights are equal to the inverses of the mean-square (positive and negative) error bars. Note that the error bars do not include the uncertainty of the telescope pointing, which – affecting all the five lines identically within the assumed model scenario – does not affect the slope (although it does affect the zero level). We also show a normalized standard deviation from the fit σ_n (for an ideal fit $\sigma_n = 0$, for deviations ideally consistent with the errors $\sigma_n = 1$, and when the measurements deviate from the model $\sigma_n > 1$). The full dataset is presented in Fig. 12 (see *online version*).

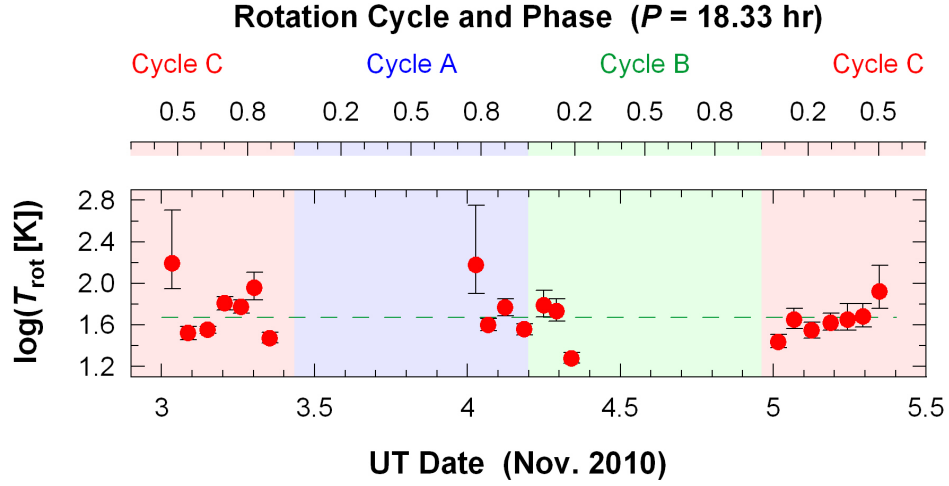


Fig. 4.— Variation of the logarithmic rotational temperature $\log(T_{\text{rot}})$ with time, derived from the time series of CH_3OH . The green dashed line indicates the temperature level of 47 K obtained from the mean spectrum (Figs. 1 and 6). The additional top axis shows the nucleus rotation phase and *three-cycle* component (cf. Paper I), and the latter is also coded by the background color. The *EPOXI* flyby occurred on UT 2010 Nov. 4.5832, corresponding to phase 0.5 of *Cycle B*.

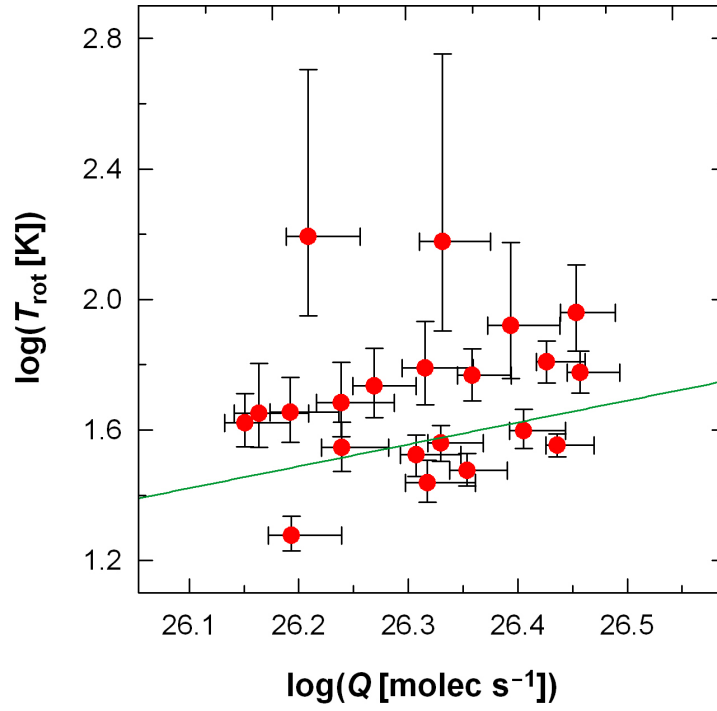


Fig. 5.— Tentative positive correlation of the rotational temperature T_{rot} (Fig. 4) and the production rate Q (Fig. 8), derived from the time series of CH_3OH , and presented in a log–log space. The weighted linear fit has a slope 0.67 ± 0.25 .

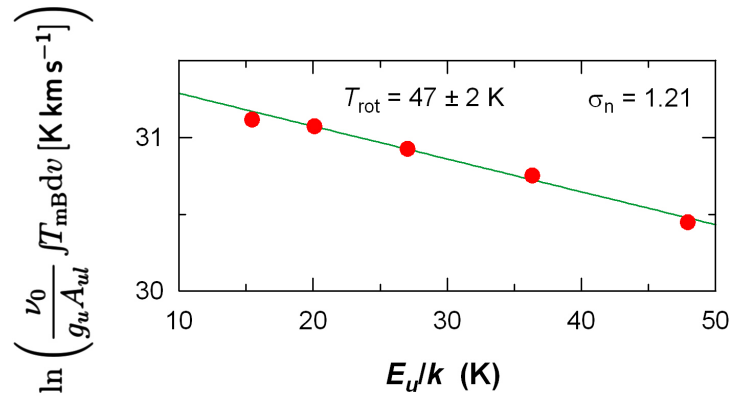


Fig. 6.— Rotational diagram for the mean spectrum of CH₃OH from Fig. 1. The error bars are smaller than the symbol size. Other details are the same as in Fig. 3.

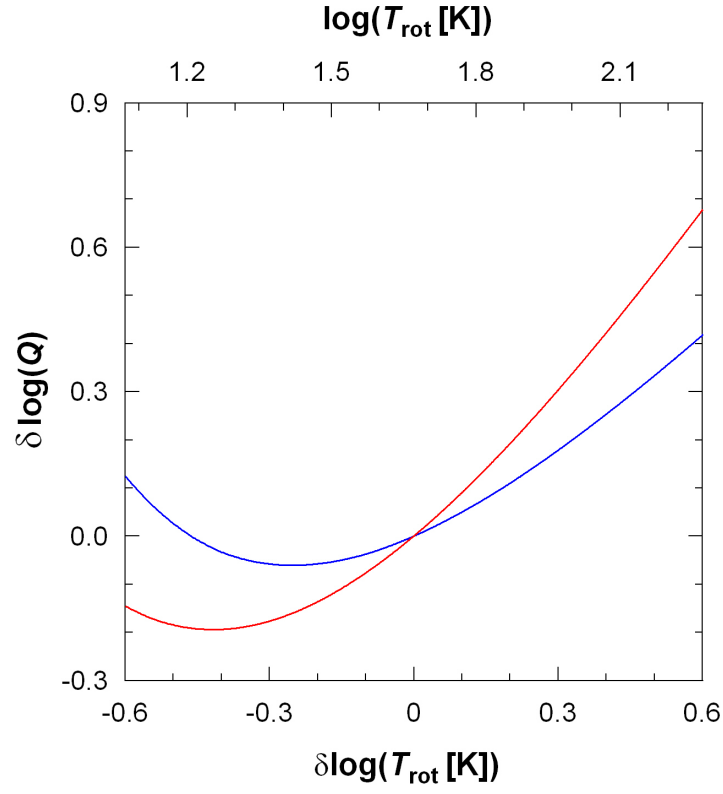


Fig. 7.— Dependence of the derived production rate Q on the adopted rotational temperature T_{rot} , presented as logarithmic offsets applicable to CH_3OH (red) and HCN (blue). The absolute logarithmic temperature scale is given by the upper horizontal axis.

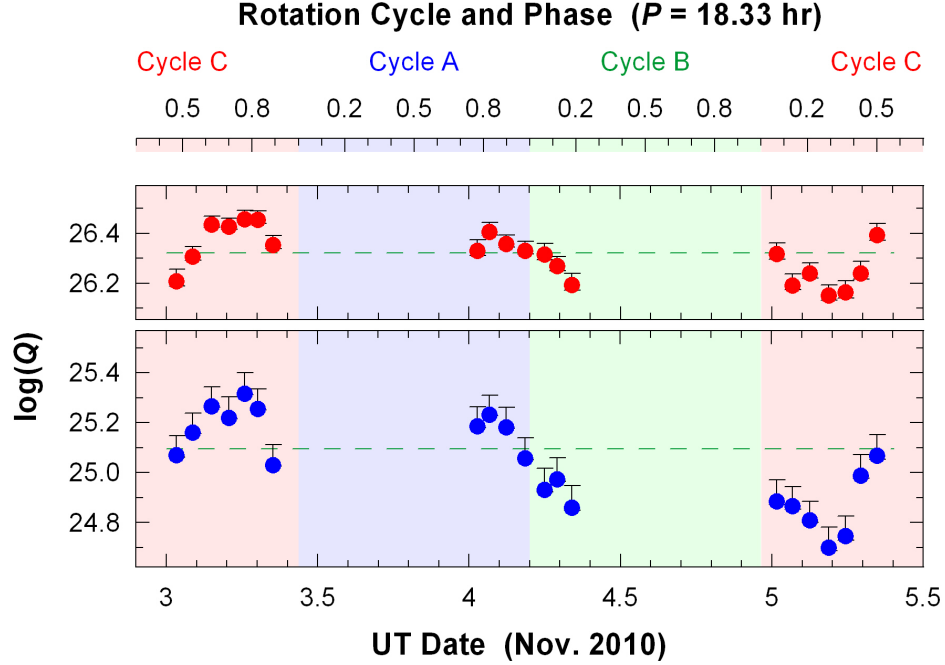


Fig. 8.— Production-rate variability in CH_3OH (red symbols in *top panel*) and HCN (blue symbols in *bottom panel*). The logarithmic production rates $\log(Q)$ vary about the average values: 2.10×10^{26} molec s^{-1} for CH_3OH and 1.25×10^{25} molec s^{-1} for HCN (green dashed lines). The asymmetry of the error bars results from the uncertainty of the telescope pointing (cf. Paper I) which surpasses the errors from noise. For this reason, the uncertainties on the simultaneously-measured CH_3OH and HCN are partly correlated, unlike the errors on subsequent points. Systematic errors affecting only the absolute levels (introduced by, e.g., the uncertainties of the rotational temperature and gas velocity, or the errors on the molecular constants) were neglected because they do not change the shapes of the variability profiles. The additional top axis shows the nucleus rotation phase and *three-cycle* component (cf. Paper I), and the latter is also coded by the background color. The *EPOXI* flyby occurred on UT 2010 Nov. 4.5832, corresponding to phase 0.5 of *Cycle B*.

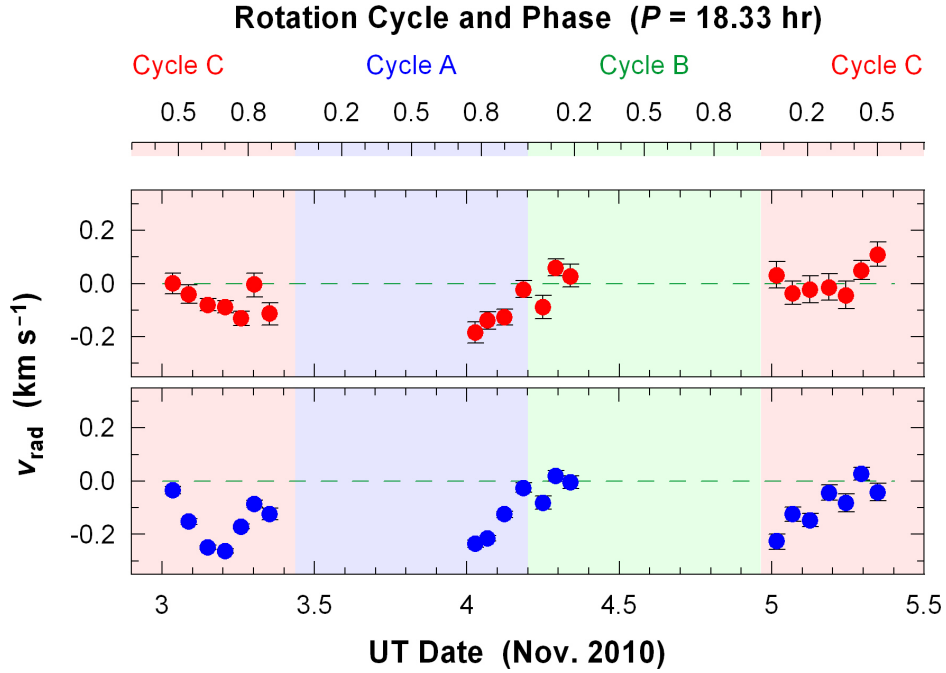


Fig. 9.— Variability of the median radial velocity v_{rad} in CH_3OH (red symbols in *top panel*) and HCN (blue symbols in *bottom panel*) about the rest velocity (green dashed lines). The uncertainty of the telescope pointing is assumed to have a negligible influence on this parameter and hence the errors result entirely from noise (cf. Paper I). The additional top axis shows the nucleus rotation phase and *three-cycle* component (cf. Paper I), and the latter is also coded by the background color. The *EPOXI* flyby occurred on UT 2010 Nov. 4.5832, corresponding to phase 0.5 of *Cycle B*.

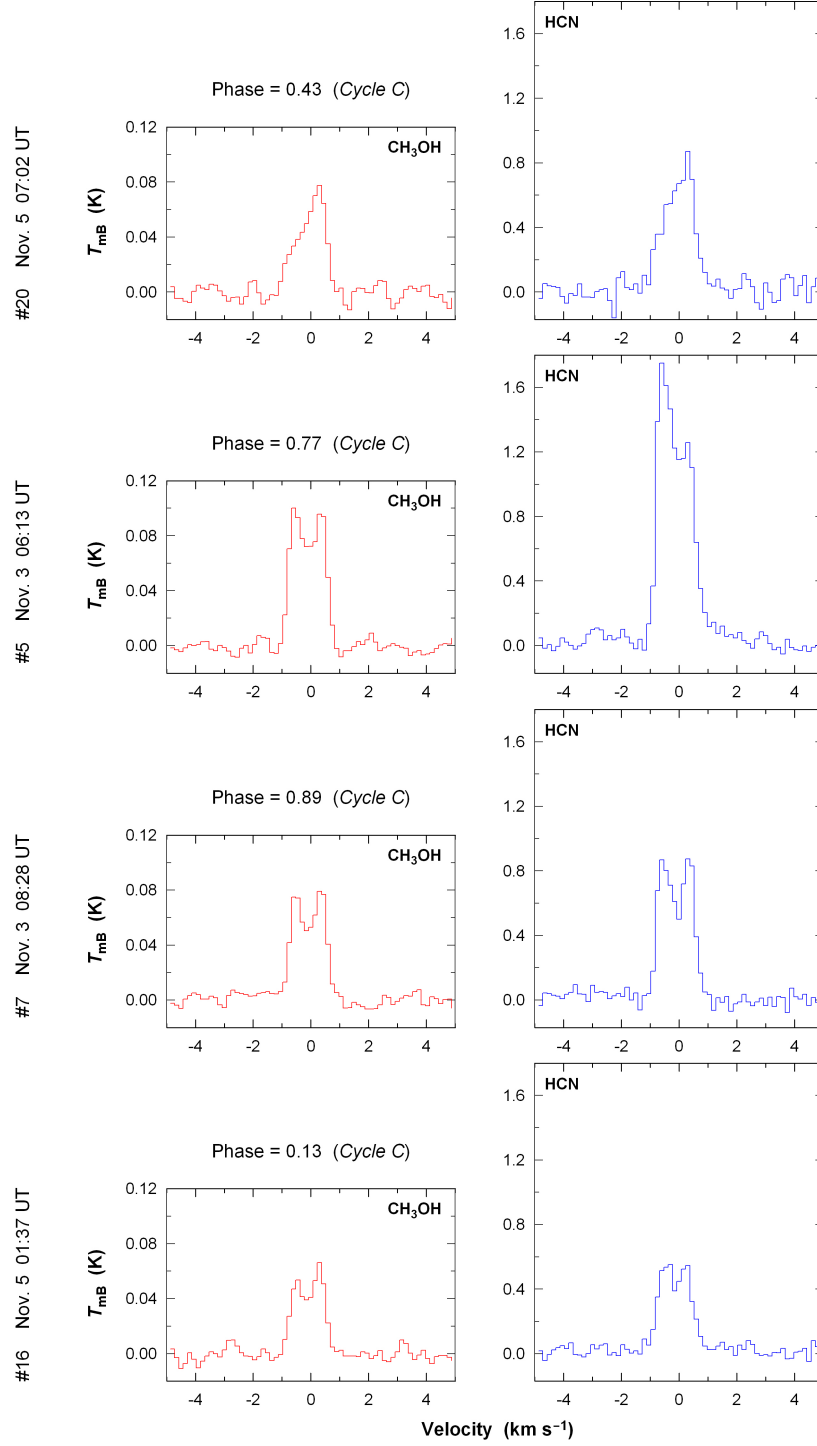


Fig. 10.— Examples of the line profiles of CH_3OH (left) and HCN (right) illustrating the temporal variations. The former are the mean profiles from the observed 5 lines whereas the latter are the profiles of the $J(3-2)$ transition (Section 2 and Table 1). We selected four representative rotation phases from two consecutive *Cycles C* (cf. Paper I) observed on UT 2010 Nov. 3 (*middle panels*) and Nov. 5 (*top and bottom*). The full dataset is presented in Fig. 13 (see *online version*).

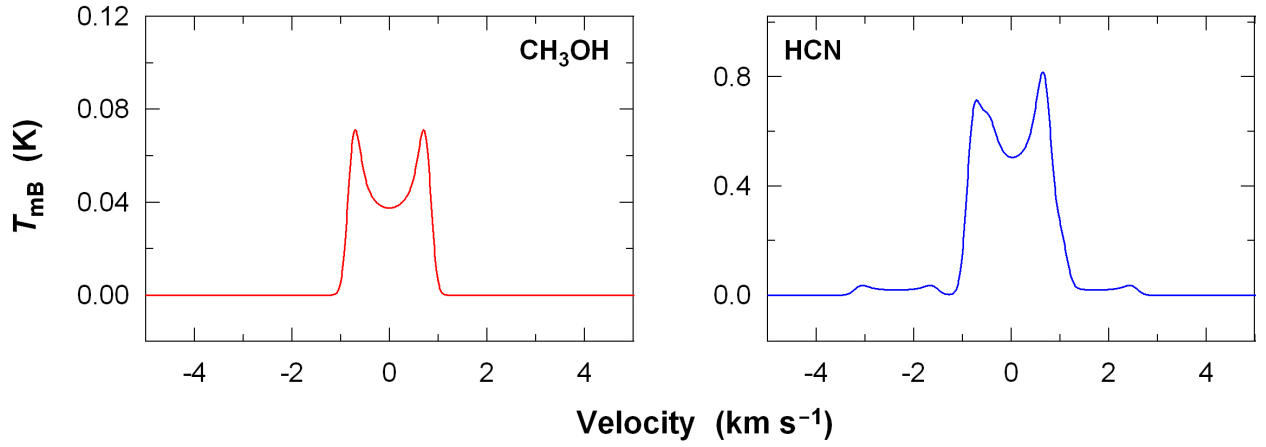


Fig. 11.— Simulated spectra of CH₃OH (*left*) and HCN (*right*) corresponding to our observations (cf. Fig. 10). We assumed a steady-state isotropic production from a central source at the measured average rates of 2.10×10^{26} and 1.25×10^{25} molec s⁻¹, respectively (Section 4.1), a constant gas-flow velocity of 0.8 km s⁻¹ (Appendix A), and LTE at 47 K (Section 3). The beam sizes and the molecular constants were used the same as given in Table 1 (Section 2). The HCN profile additionally accounts for the hyperfine structure taken from the Cologne Database for Molecular Spectroscopy (Müller et al. 2005), which introduces the asymmetry. This information is currently unavailable for the observed lines of CH₃OH hence the mean model profile is symmetric.

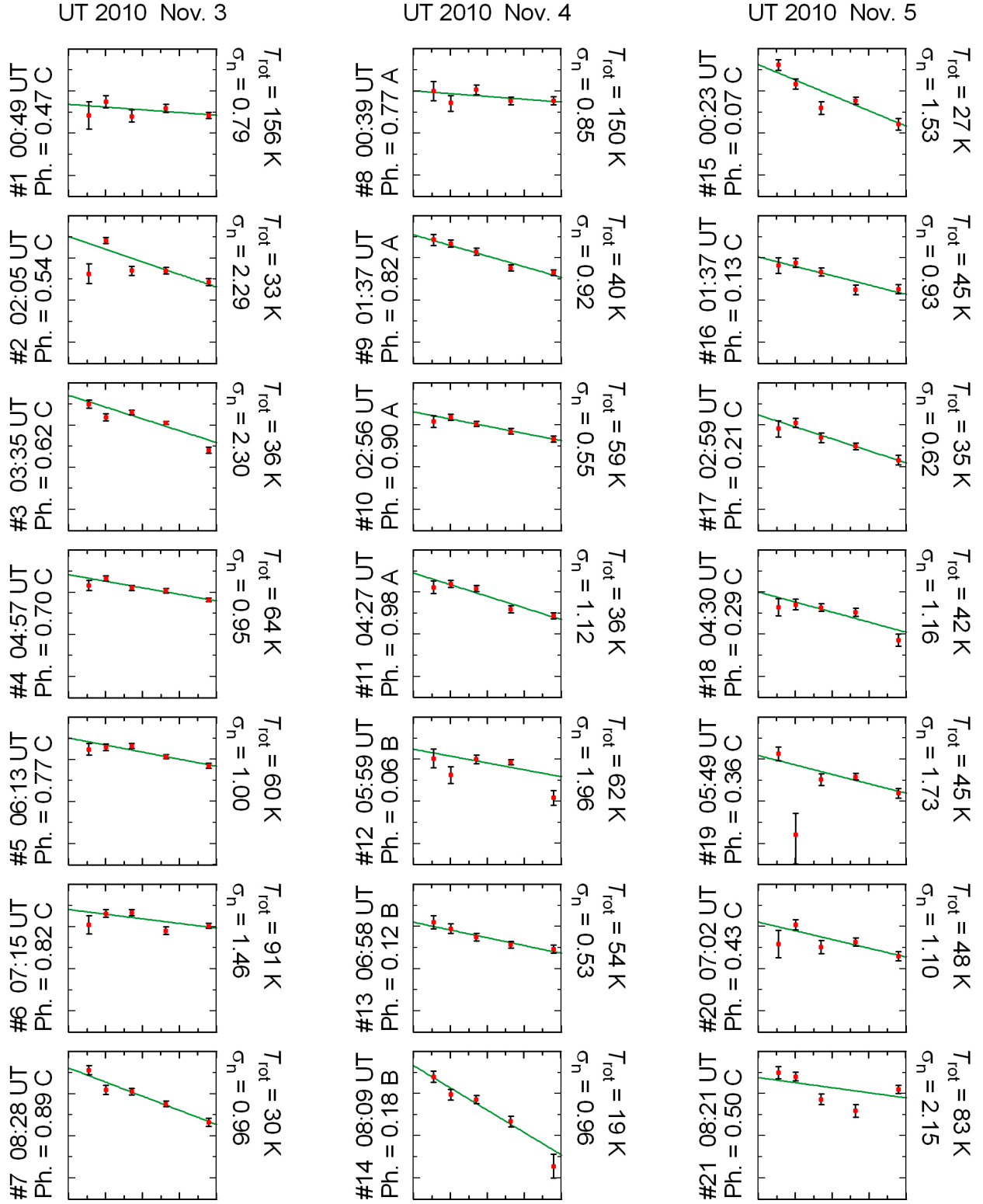


Fig. 12.— Full set of the 21 rotational diagrams derived from the time series of CH_3OH , with weighted linear fits. Other details, including figure axes, are the same as in Fig. 3. This material is also contained in Animation 1.

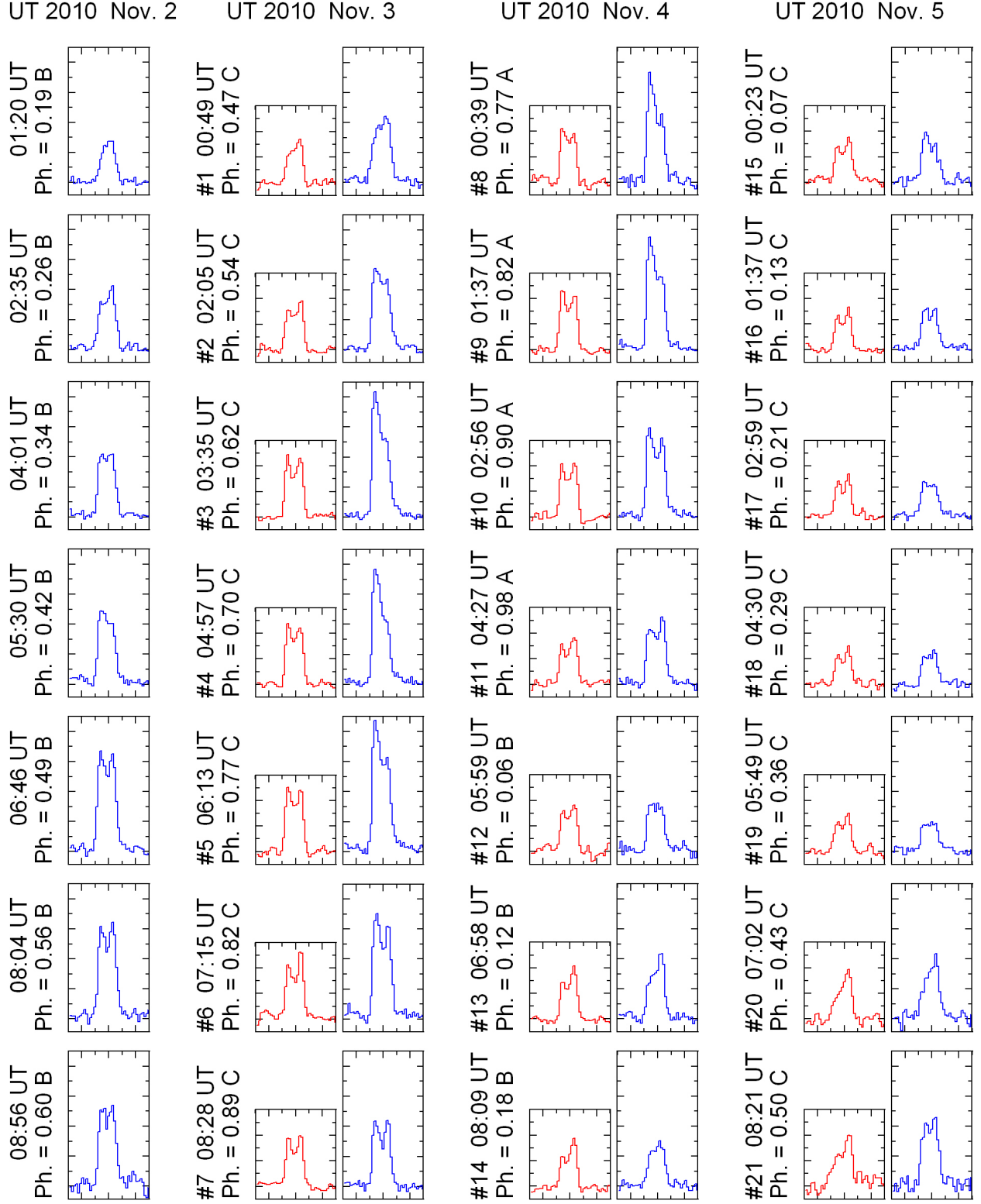


Fig. 13.— Full set of the 28 line profiles of HCN (*blue*) and 21 line profiles of CH₃OH (*red*) illustrating the temporal variations. Other details, including figure axes, are the same as in Fig. 10. This material is also contained in Animation 2.

Table 1. Transition and Telescope Constants

Molecule	Transition	ν_0^a (GHz)	A_{ul}^b (10^{-6} s^{-1})	g_u^c	E_u/k^d (K)	Beam ^e ($''$) ^f	(km) ^g	τ_\perp^h (min)	Δv^i (m s^{-1})	η_{mB}^j
HCN	$J(3-2)$	265.886434	838.40	21	25.521	4.4	495	10.3	44	0.52
CH ₃ OH	$5_{0,3}-5_{1,4}$	157.179017	40.77	11	47.934	7.4	826	17.2	149	0.72
	$4_{0,3}-4_{1,4}$	157.246056	41.97	9	36.335					
	$1_{0,3}-1_{1,4}$	157.270851	44.11	3	15.447					
	$3_{0,3}-3_{1,4}$	157.272369	42.94	7	27.052					
	$2_{0,3}-2_{1,4}$	157.276058	43.64	5	20.090					

^aTransition rest frequency from the Cologne Database for Molecular Spectroscopy (CDMS; see Müller et al. 2005), available online at <http://www.astro.uni-koeln.de/cdms>.

^bEinstein coefficient for spontaneous emission from the High-resolution Transmission Molecular Absorption Database (HITRAN; see Rothman et al. 2005), available online at <http://www.cfa.harvard.edu/hitran>. We note that the values for the five lines of CH₃OH, derived from the *integrated intensity* in the JPL Molecular Catalog (<http://spec.jpl.nasa.gov>, Pickett et al. 1998), are consistently ~ 3 times lower, while the value for HCN $J(3-2)$ is 7% higher. While we adopt the HITRAN values, these inconsistencies have obvious implications for the absolute production rates discussed in Section 4.1 (cf. Appendix A); they are, however, of no importance for any other result presented in this work.

^cDegeneracy of the upper state g_u from CDMS.

^dUpper state energy E_u obtained from CDMS.

^eHWHM of the beam.

^fAngular beam size.

^gBeam size at the comet distance.

^hMinimum escape time from the beam needed to reach HWHM at a constant velocity 0.8 km s^{-1} .

ⁱNative velocity spacing of the spectral channels.

^jMain-beam efficiency interpolated from the values given at <http://www.iram.es/IRAMES/mainWiki/Iram30mEfficiencies>.